POLITECNICO
MILANO 1863

DIPARTIMENTO DI MECCANICA

mecc

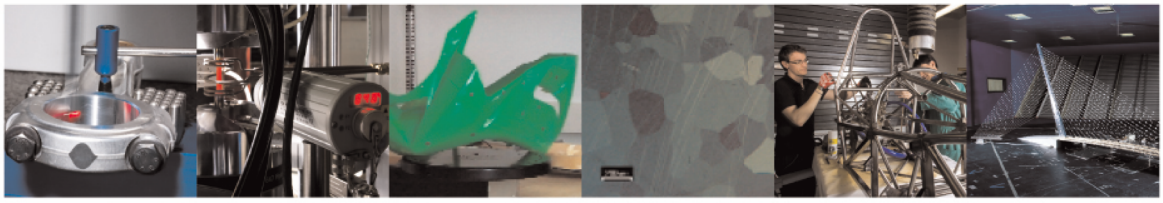

A Numerical Framework to Design and Develop Freestanding Porous Structures through Cold Spray Multi-Material Deposition

Terrone M.; Ardeshiri Lordejani A.; Kondas J.; Bagherifard S.

This is a post-peer-review, pre-copyedit version of Matteo Terrone, Amir Ardeshiri Lordejani, Jan Kondas, Sara Bagherifard, *A numerical Approach to design and develop freestanding porous structures through cold spray multi-material deposition*, Surface and Coatings Technology, Volume 421, 2021, 127423.
https://doi.org/10.1016/j.surfcoat.2021.127423.

DIPARTIMENTO DI MECCANICA ■ POLITECNICO DI MILANO
via G. La Masa, 1 ■ 20156 Milano ■ EMAIL (PEC): pecmecc@cert.polimi.it
http://www.mecc.polimi.it
Rev. 0

A Numerical Framework to Design and Develop Freestanding Porous Structures through Cold Spray Multi-Material Deposition

Matteo Terrone[a], Amir Ardeshiri Lordejani[a], Jan Kondas[a,b], Sara Bagherifard[a]

[a]Department of Mechanical Engineering, Politecnico di Milano, Milan, Italy
[b]Impact Innovations GmbH, Bürgermeister-Steinberger-Ring 1, 84431, Haun/Rattenkirchen, Germany

1 Abstract

Cold spray is a solid-state particle deposition technique with a wide range of applications for coating, repair and additive manufacturing. Cold spray parameters are normally tuned to obtain deposits with minimal porosity and thus highest strength. However, there are specific applications such as biomedical prostheses, heat sinks and energy absorbing products, where a higher exposed surface area can lead to enhanced performance, rendering porosity a desirable feature. Few recent studies have experimentally evaluated the potential of cold spray technology for obtaining porous deposits. To enhance the efficiency of these approaches, here we developed a detailed numerical framework that can determine the topological and mechanical features of cold spray porous deposits. A series of combined Eulerian-Lagrangian finite element models were developed considering a multi-material feedstock, one constituent of which served as a porogen. Different powder blends of pure Ti mixed with either Al or Cu, as the sacrificial powder, with varying volumetric fractions were analysed. A novel post-processing approach was developed to remove the sacrificial powder and extract distinct characteristic indicators from the simulations' output; these indices include porosity and structural connectivity of the remaining Ti structure. Equivalent plastic strain was considered as an index to assess the strength of the resultant deposit. The obtained data regarding particle deformation were in agreement with preliminary experimental tests. The numerical results revealed that Ti-Cu combinations can yield deposits with higher Ti particle deformation compared to the Ti-Al blend and hence, lead to a better inter-particle bonding. Our study presents a robust numerical approach for selection of cold spray process parameters towards obtaining coatings and freestanding porous metal parts with modulated porosity, connectivity and strength.

Keywords: Cold spray, Finite element method, Porosity, Connectivity, Coupled Eulerian Lagrangian, Sacrificial powder, Porogen, Additive manufacturing.

2 Introduction

Cold spray (CS) is a solid state deposition method in which micron-scale powder particles of 20-100 µm in diameter are accelerated to velocities up to 500-1200 m/s by a supersonic gas stream passing through a De Laval nozzle [1]. Upon impacting the substrate surface, particles undergo plastic deformation and adhere to the substrate and subsequently to the already bonded powder at solid state, forming a dense deposit. Its unique features, including the low process temperature, promote the application of CS for creating thick deposits of various materials on a wide range of substrates; this makes CS suitable for depositing protective coatings, spot repair and maintenance of defected parts, and more recently additive manufacturing of load bearing structures [2,3]. This intrinsic flexibility allows for modulating deposit properties across its thickness; the gradient properties can be tuned based on the target application to modulate mechanical properties and the interaction of the deposit with the surrounding environment. Designing a porous coating is a representative case where having a porous external layer and a solid core can be beneficial for a range of applications such as mass transfer, wave absorption [4], electrochemical electrodes [5] or orthopaedical implants. Traditional routes to obtain porous metallic objects include plasma or flame spray [6,7], additive manufacturing [8], combustion sintering [8], chemical or arc vapor deposition using a space holder (polymeric spheres or foams), or powder metallurgy methods and sintering [9,10]. Majority of these techniques are high temperature processes that induce large residual stresses, undesired phase transformations, recrystallization, oxidation or contamination in the fabricated porous object; they are also highly restricted regarding the final size of the deposit. Unlike these technologies, CS obtains bonding through plastic deformation at a low thermal input and thus avoids almost all the above-mentioned issues upon deposition. Additionally, CS can offer significantly higher flexibility in terms of deposit dimensions and is also characterized with a much higher build up rate (e.g., 10-14 times higher than common powder bed additive manufacturing [11]).
Particles in CS adhere to the substrate and form a dense coating if they are accelerated to a "critical"

velocity that is a function of the powder's thermo-mechanical properties. One approach to get porous deposits using CS is to adjust the key process parameters, such as standoff distance, particles' shape and size, gas stagnation pressure and temperature, nozzle transverse speed and substrate temperature. This approach to obtain porous CS deposits is based on working at velocities lower than the critical range to reduce the probability of adhesion for all impacting particles; implementing this method will lead to substantially low deposition efficiency (DE) and limited control on porosity and connectivity. An alternative approach to achieve CS deposits with modulated porosity and desirable mechanical properties is to include a sacrificial material in the feedstock powder, which will be removed using a post-deposition treatment for example chemical etching or thermal processes, such as vaporization or diffusion [5,12–15]. In this way, it is possible to control the porosity level while still achieving favourable mechanical properties for the deposit.

Regarding the latter approach that offers the opportunity to modulate the porosity, it should be noted that CS deposition of multi-material feedstock requires careful selection of many interconnected process parameters; these are affected by the choice of powder materials, their particle size distribution, and respective volume fractions. If thermo-mechanical properties of the two constituent materials are notably different, finding the proper process parameters that would provide the suitable condition for achieving critical velocity for both powder types will be quite challenging [16]. Considering these complexities, as a common practice, the process parameters for multimaterial depositions are chosen based on experimental trials. Thus, numerical simulations can provide notable advantages in this regard by substantially reducing the experimental effort and the related costs.

Since early on, various numerical tools have been adopted to simulate different aspects of CS process. The initial efforts, which are continuing to evolve till now, were focused on determination of critical velocity for different powder-substrate combinations [1,17,18], along with the evolution of residual stress in the coating and substrate [19–21]. Other researches started to employ FE for investigating the other parameters that affect the efficiency of CS deposition such as substrate temperature [22]. Numerical models have been also adapted to predict the grain boundary and crystalline structure of the final resultant coating, which will be determined in part by the mesoscale deformation of particles, depending on the selection of process parameters [23].

A survey of the present literature, along with a familiarity with different available formulations for finite element (FE) reveals their distinct and unique capabilities, each of which can be associated with a different aspect of the CS deposition process. Among the present body of research in the field of FE simulation of CS process the Lagrangian [24–27], arbitrary Lagrangian-Eulerian (ALE) [21,28–33], smoothed particle hydrodynamics (SPH) [29,34,35] and coupled Eulerian-Lagrangian (CEL) [36–38] are the prominent and most-investigated formulation methods.

However, due to the innate complexity of the CS process, prohibitive computation costs and the constraints of the simplifying assumptions in some of the FE formulations, a major part of the research has been focused on numerical simulation of impact and bonding of a single, or a small number of particles to the substrate.

In the recent years, researchers have tried to validate and employ the capabilities of different aforementioned FE formulations. Shayegan et. al [21] and Yin et. al [39] were able to simulate the CS impact of 10 to 40 particles and validate their FE results against the experimental data, exhibiting the capabilities of well-known FE formulations to model the multi-particle impact in CS. Lee et. al. [29] were able to integrate a damage prediction model, while simulating the impact of about 90 particles using SPH formulation [29]. Instead, Saleh et. al. could significantly increase the number of considered particles in an SPH model without considering the damage. Ghelichi et. al. [25] were among the first to consider a precise representation of the R-R particle size distribution in their model. Song et. al. [36] proposed the capability of CEL FE method to simulate the CS deposition of a large number of particles with the ability to consider an accurate size distribution. However, among the discussed studies, none have simulated the deposition of a multi-material feedstock.

This paper presents a systematic FE scheme for simulating CS deposition using multi-material feedstock, aimed at developing modulated porosity for any given set of materials and adopted CS parameters. The obtained results are then post-processed to extract and propose several parameters that assess the porous structure topology and its strength. With this framework, it is possible to numerically evaluate the optimized CS settings, hence drastically reduce the number of the required tests and the experimental costs incurred.

We adopted our developed methodology to compare CS deposits obtained from spraying two sets of

material combinations, namely Ti-Al and Ti-Cu, in which Al and Cu act as sacrificial materials. We also compared the results in terms of qualitative particle deformation with some preliminary experimental trials of cold sprayed Ti-Al deposits. Both Al and Cu can be chemically dissolved after deposition, using commercially available chemical solutions that have no effect on Ti structure at room temperature [13,15,40–42]. These sacrificial materials are much more deformable than Ti, and their content, along with other process parameters, can be controlled to tailor the topological and mechanical properties of the remnant porous structure, without having major drawbacks on inter-particle adhesion of the Ti particles.

3 Numerical model development

CS process can be modelled as a sequential ballistic impact of metallic powder particles on a substrate. As described before, in the literature, several different FE techniques are proposed to model the space discretization for simulation of CS process. Xie at al. [43–46] compared all the different approaches for a single particle impact and concluded that the CEL approach provides the most robust and accurate solution for CS simulation. Unlike the conventional Lagrangian method, a CEL model consists of both an Eulerian and a Lagrangian domain. In the Eulerian domain, the material is not constrained to a predefined element discretization; instead, it can freely flow through a stationary element discretized domain and each element at any given time can contain a specific amount of material, which is indicated by a volumetric fraction index ranging between 0 and 1. This allows for simulation of models with high deformation extents without distortions and inaccuracies of other Lagrangian models.

The basis of the FE model developed here using Abaqus 2017 commercial software, is similar to the model proposed by Song [36]. The CEL approach was implemented, in which the particles were defined using an Eulerian space discretization and the substrate as a Lagrangian domain. Explicit dynamic temperature-displacement analysis was developed for systems of around 200 particles for both Ti-Cu and Ti-Al combinations, with different volumetric mixtures. Figure 1 shows a representative model for 50-50% volume fraction of Ti-Cu blend. An Al substrate at room temperature of 300º K was considered for all simulations. It should be noted that due to the operational constraints of CEL formulation, the effect of DE for each individual powder constituent was not considered in the model. Different aspects of the model are described in detail in the following sections.

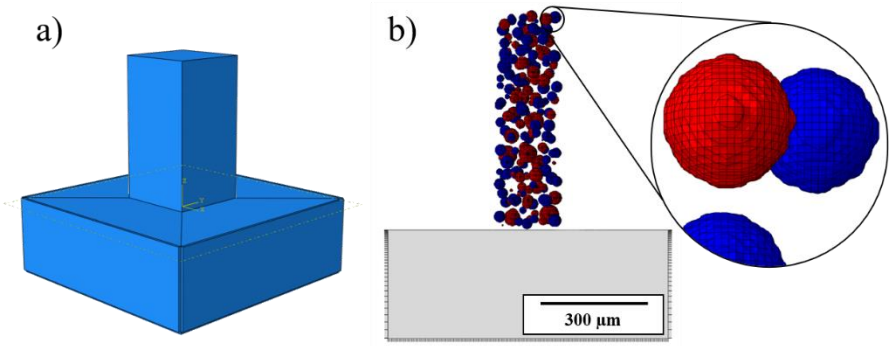

Figure 1: a) CS assembled model with the Eulerian parallelepiped domain on top and the Lagrangian substrate at the bottom, b) Random arrangement of a multi-material feedstock representative model with 50-50% V/V at t=0 (distinct colors refer to two different metals)

It is worth mentioning that a perfectly spherical powder was considered as the simulated morphology, and the aliased surface of the magnified particles in the insert in Figure 1 is due to the required filtration of Eulerian domain elements based on their material content, which will be discussed in the next sections.

3.1 Material and contact properties

The CS process consists of multiple non-linear dynamic impacts, involving high strain rate plastic deformation and temperature change. To accurately simulate this phenomenon, the effects of temperature, strain rate and hardening on the particle and substrate deformation should be considered in the respective material properties. In this work, these aspects were implemented using the Mie-Grüneisen equation of state (EOS) and rate-dependant Johnson-Cook plasticity model. The erosion and cracking process, happening at a very high impact velocity, were neglected and no failure or damage model was implemented.

The Mie-Grüneisen EOS was adopted to describe the linear elastic response of the materials with the following equation that relates the pressure p to the density ρ [47,48]:

$$p = \frac{\rho_0 c_0^2 \eta}{(1 - s\,\eta)^2}\left(1 - \frac{\Gamma_0 \eta}{2}\right) + \Gamma_0 \rho_0 e_m \tag{1}$$

Where:

- Γ_0 is the Grüneisen material constant
- e_m is the internal energy per mass unit
- ρ_0 is the reference density
- c_0 and s are material constants that define the linear relationship between the shock velocity and the particle velocity
- η is the nominal volumetric compressive strain and it is equal to $\eta = \left(1 - \frac{\rho_0}{\rho}\right)$

The adopted EOS parameters for all the materials are reported in Table 1.

Table 1: EOS parameters for Ti, Al and Cu [30,35,46,49]

		Ti	Al	Cu
c_0 [m/s]	Sound velocity	4779	5386	3940
s	Slope in U_s versus U_p	1.089	1.339	1.489
Γ_0	Grüneisen coefficient	1.18	1.97	2.02

The plasticity was assumed to be governed by the Johnson-Cook (JC) plasticity model with temperature and strain rate dependency [48,50]. In Johnson-Cook model, the stress σ_{J-C} is defined as:

$$\boldsymbol{\sigma_{J-C}} = [\boldsymbol{A} + \boldsymbol{B}\,\boldsymbol{\varepsilon^n}]\left[\mathbf{1} + \boldsymbol{C}\,\ln\left(\frac{\dot{\boldsymbol{\varepsilon}}}{\dot{\boldsymbol{\varepsilon}}_{\mathbf{0}}}\right)\right]\left[\mathbf{1} - \hat{\boldsymbol{T}}^{\boldsymbol{m}}\right] \tag{2}$$

With $\hat{T}$ being a non-dimensional temperature defined as:

$$\hat{T} = \begin{cases} 0 & \text{for } T < T_t \\ \dfrac{T - T_t}{T_m - T_t} & \text{for } T_t \le T \le T_m \\ 1 & \text{for } T > T_m \end{cases} \tag{3}$$

Where ε is the equivalent plastic strain, $\dot{\varepsilon}$ is the equivalent plastic strain rate, $\dot{\varepsilon}_0$ is the reference plastic strain rate, T_m is the melting temperature of the material and T_t is the transition temperature defined as the one at or below which there is no temperature dependence of the yield stress. Coefficient A is the yield strength, B is the hardening modulus, C is the strain rate sensitivity coefficient, n is the hardening coefficient and m is the thermal softening coefficient.
All of parameters for the JC plasticity model of the three utilized materials are listed in Table 2.

Table 2: Johnson-Cook plasticity parameters for Ti, Al, and Cu [30,31,46,49,51]

		Ti	Al	Cu
A [MPa]	Yield stress	806.57	148.4	90
B [MPa]	Hardening constant	481.61	345.5	292
n	Hardening exponent	0.319	0.183	0.31
m	Thermal softening exponent	0.655	0.895	1.09
T_m [K]	Melting temperature	1923	916	1356
T_t [K]	Transition temperature	298	293	298
C	Strain rate constant	0.0194	0.001	0.025
$\dot{\boldsymbol{\varepsilon}}_{\mathbf{0}}$	Reference strain rate	1	1	1

Other material parameters (namely thermal conductivity, density, shear modulus, and specific heat) were required to solve the heat transfer and dynamic/kinetic equations. The temperature dependant values of these parameters were extracted from the material property database (MPDB) provided by

JAHM Software, Inc [52]. However, for the sake of brevity only the values for room temperature data are reported here Table 3. The inelastic heat fraction for CS was assumed equal to 0.9 [1,46]. The latent heat was neglected to avoid its significant nonlinearity that would result in artificially induced incorrect energy peaks.

Table 3: Material properties at room temperature (300K) [52]

		Ti	Al	Cu
$\boldsymbol{\rho}$ *[kg/m³]*	Density	4499	2698	8939
$\boldsymbol{G}$ *[MPa]*	Shear modulus	40634	25889	47364
$\boldsymbol{c}$ *[J/(kg·K)]*	Specific heat	523.9	898.2	383.62
$\boldsymbol{\lambda}$ *[W/(m·k)]*	Thermal conductivity	21.129	237.2	315.82

Multiple interactions were defined in the model to describe the interaction between individual particles and also with the substrate. Surface-to-surface contacts were assigned to define the interaction between each material and the substrate, while a general contact determined the interaction between particles. All the interaction properties considered a hard contact in the normal direction, while allowing separation after contact. They all assumed that the generated heat constituted 90% of the energy [46]. The tangential behaviour was modelled with a penalty formulation of friction considering different coefficients of coulomb friction, the values for which are reported in Table 4 [46]. It should be mentioned that the intrinsic interaction between the Eulerian material instances is sticky and no slip or separation occurs at the Eulerian body interfaces [48]. Therefore, the particles could not rebound from the deposit, leading to a full deposition DE.

Table 4: Coulomb friction coefficients used in Ti-Al and Ti-Cu simulations [53,54]

	Ti-Al	Ti-Cu
$\mu_{\text{Between particles}}$	0.43	0.43
$\mu_{\text{Sacrificial material-Substrate}}$	0.8	0.23
$\mu_{\text{Ti-Substrate}}$	0.32	0.32

4 Particle arrangement

To provide an accurate representation of the actual deposition process, particles within the Eulerian domain were generated following a Rosin-Rammler (R-R) size distribution based on the data provided by the corresponding suppliers, with their positions being randomly allocated to avoid any overlap. The R-R distribution, represented by Eq.4, is a common way to describe the size distribution of feedstock powder [55–58]:

$$\boldsymbol{R(d) = 100\, e^{-\left(\frac{d}{d'}\right)^{n}}} \quad (4)$$

In which d is the particle size, $R(d)$ is the cumulative percentage of material powder with the corresponding particle size d, d' is the mean particle size (i.e., size parameter), and n is a measure of the particle size spread (i.e., distribution parameter); a smaller n value means a wider powder size distribution. Therefore, the size distribution of an intended powder can be described, given the value of d' and n. These parameters were evaluated by comparing different pairs of $R(d)$ and d in the R-R distribution to find the best fit. The considered $R(d)$ and d pairs were taken from datasheet provided by suppliers of commercially available powders (Table 5). All the considered powders are spherical and produced with atomization technique. The obtained R-R parameters for each powder are shown in Table 6 and the powder distribution is represented in Figure S1.

Table 5. Particle size distribution data used to evaluate Ti, Al, and Cu R-R distribution provided by suppliers

	D10 [μm]*	D50 [μm]*	D90 [μm]*
Ti Gd2 (TLS, Germany)	15.06	33.28	48.68
Al CG (GMBH, Germany)	19.61	34.32	60.93
Cu (Safina, Czech Republic)	18	29	40

*****Values of D10, D50 and D90 indicate that 10, 50 and 90% of the particles have a diameter smaller than the mentioned sizes, respectively.

Table 6. Calculated R-R parameters for Al, Ti and Cu powders

	d'[mm]	n
Al	41.299	2.5098
Ti	37.206	2.8561
Cu	31.355	3.8627

Definition of process parameters was supported by simulations performed using the commercial software package from Kinetic Spray Solutions (KSS GmbH, Buchholz, Germany) [59] assuming nitrogen as the propellant gas. In all the simulations, the OUT1 (Impact Innovation GmbH, Germany) was selected as the nozzle with an expansion ratio of 5.6 and a total length of 160 mm. KSS software estimates the variation of particle impact velocity and temperature for each particle diameter, based on computational fluid dynamic (CFD) simulations of the two-phase flow through the nozzle and the free jet, for each set of process parameters, including powder material, stagnation pressure and temperature. More details on the KSS calculations are available in [60,61]. The temperature and velocity variation trends were then accurately fitted by third order polynomial functions using a Python code [62]. The KSS software simulations were run with stagnation pressures of 50 and 30 bars, and temperatures of 750 °C and 500 °C for Ti-Cu and Ti-Al powder mixtures, respectively. The selected pressure and temperature for the Ti-Al cases were set comparatively lower to account for the practical issues associated with nozzle clogging by Al in experiments [63,64]. Figure 2 shows the predicted trends of particle impact velocity and temperature for each material in both powder mixtures. The fitted polynomial coefficients are listed in Tables S1 and S2.

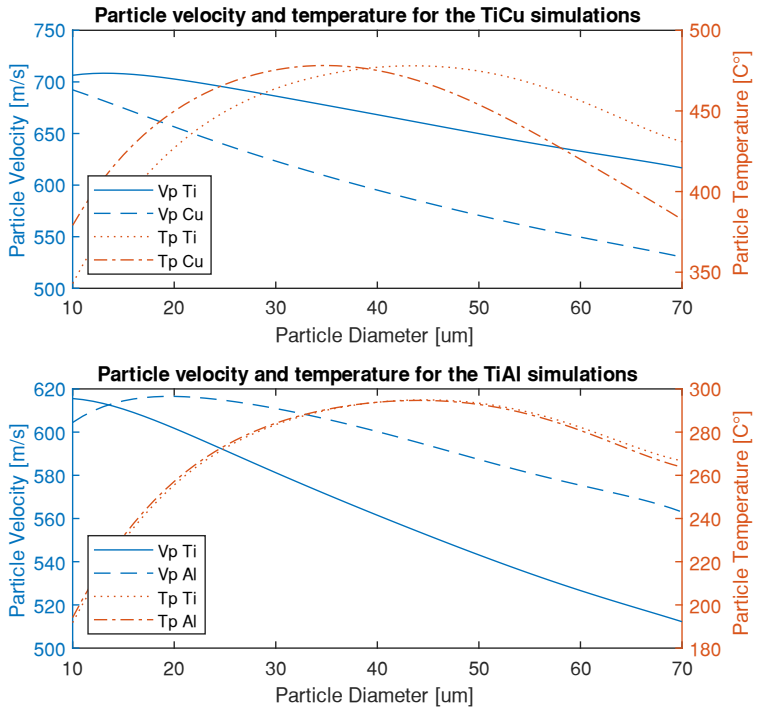

Figure 2. Estimated impact particle velocity (V_p) and temperature (T_p) as a function of particle diameter, obtained from KSS simulations

4.1 Model construction

A customized algorithm was implemented with a Python script to automatically construct the multi-particle model. The inputs of the script are the number of particles for one constituent phase and the corresponding volume percentage in the feedstock powder. The algorithm computes the particles size according to the R-R distribution using the corresponding d' and n values for each material (Table 6); and then, randomly positions each particle in the empty space inside the Eulerian domain, while avoiding any overlap. Occurrence of no overlap was ensured by checking if the Euclidean distance between the centroid of a new particle "n" with the centroid of all the particles "j", already set in the model, was higher than the sum of the radius of both concerned particles (R_n and R_j). The equation

below provided the mathematical description of this criterion:

$$\sqrt{(x_n - x_j)^2 + (y_n - y_j)^2 + (z_n - z_j)^2} > R_n + R_j \quad (5)$$

Where x_n, y_n, z_n are the Euclidean coordinate of the centroid of the new particle "n" and x_j, y_j, z_j are those of an already set particle "j". A particle location (x_n, y_n, z_n) was accepted only if Eq.5 was satisfied for each j going from 1 to n, or in other word, for all the particles already set in the Eulerian domain. In case a particle's location was rejected, a new one was randomly created and tested.
Next, the algorithm assigns velocity and temperature fields, correlated to individual particle diameters according to the fitted equation from KSS output. The process that is employed to evaluate the particles' location, velocity and temperature is schematized in the flowchart at Figure 3.

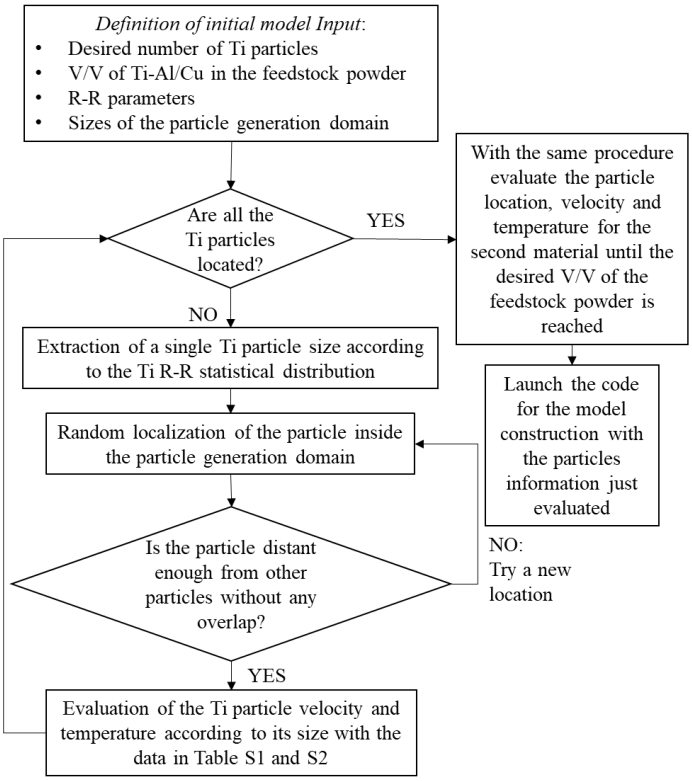

Figure 3: Flowchart for the evaluation of the particles' location, temperature, and velocity.

Regarding model discretization, the whole Eulerian domain and the Lagrangian domain near the impact zone were meshed with a regular, fine, constant cubic grid of the same size. In the Lagrangian domain, the mesh size is linearly increased towards the boundaries of the model, up to a mesh size 7 times higher than the initial one. The cuboid Eulerian domain was meshed using 3D, 8-node thermally coupled, reduced integration (EC3D8RT) elements with viscous hourglass control and second-order accuracy. The thin cuboid Lagrangian body was mostly discretized with 3D, 8-node thermally coupled, reduced integration (C3D8RT) elements with viscous hourglass and distortion control, with a length ratio parameter equal to 0.1. To avoid inaccuracies resulting from the hourglass control and reduced integration, only in the region coinciding with the Eulerian domain, a fully integrated element type (C3D8T) with second order of accuracy was employed to discretize the Lagrangian domain. In addition, thin layers of infinite elements were utilized at the external boundary regions of the substrate. These partitions were meshed with CIN3D8 element type to minimize the reflection of dilatational and shear waves back into the region of impact [25]. Therefore, the model was fixed and constrained by the infinite elements and no boundary conditions were applied on any part of the model. Due to the absence of any boundary condition on the lateral sides of Eulerian domain, the particles could freely outflow from the model without exerting unwanted stresses. However, this was foreseen and avoided by particles being generated in a smaller volume inside the Eulerian domain to allow the particles to deform inside the domain, resulting in an almost zero material outflow.

The dimension of the Eulerian domain was assumed large enough to contain all the particles. The size of the Lagrangian domain was determined accordingly, so that the substrate was 0.3 mm high, and its width was always 3 times the lateral dimension of the Eulerian domain.
For the step time incrementation, the automatic time incrementation available in Abaqus with an element-by-element approach was implemented, without any mass scaling.

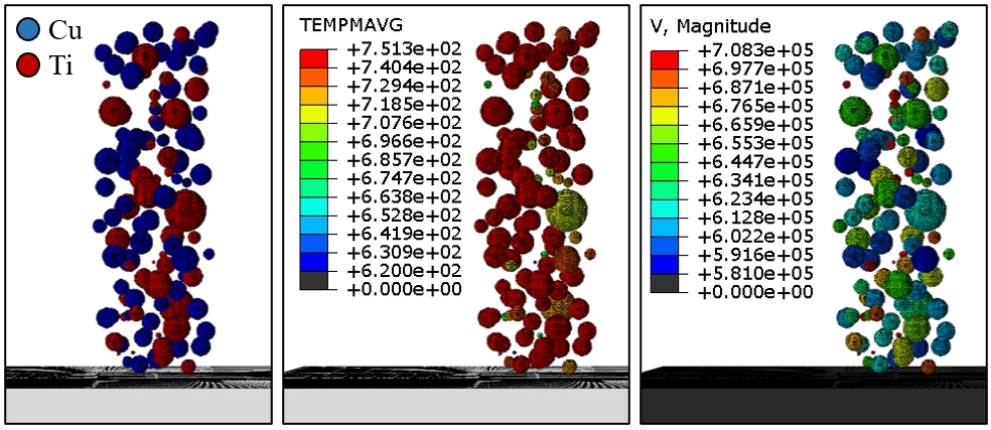

Figure 4. From left to right: material, temperature (K), and velocity (m/s) distribution at (t=0) for the Ti-Cu model with 50-50% V/V

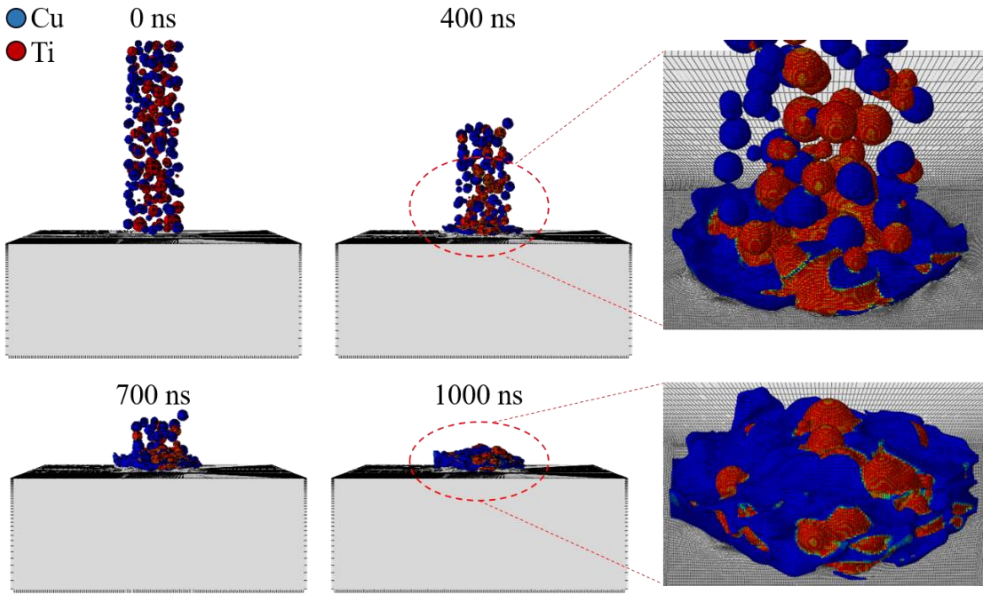

Figure 5. Snapshots of particle arrangement at different time steps for the Ti-Cu model with 50-50% V/V

4.2 Mesh Convergence Analysis

A mesh convergence analysis was performed considering different mesh sizes of 1.5, 2, 3 μm in the Eulerian domain, while keeping the rest of parameters including particles' sequence, location, dimension, velocity, and temperature constant. Table 7 shows the element numbers for each simulation and the required time to complete it.

Table 7. Simulation time, total elements number and number of used cores for the same simulation with different mesh sizes

Eulerian/Finer Mesh size	Total number of elements	Number of cores	Simulation time [h]
1.5 μm	24.636.325	30	208.33
2 μm	9.824.283	20	56.40
3 μm	2.918.220	10	16.38

The results indicated that in the Eulerian domain, the Von-Mises stresses, the equivalent plastic strain

(PEEQ), and the plastic strain in the principal direction (PE) stabilized for mesh sizes lower than 2 μm. A similar result was obtained by Song et al. [36]. Instead, in the Lagrangian domain, a linear variation was obtained for both strain (PEEQ and PE) and Von-Mises stress with no clear convergence point, which is in line with available studies on the FE simulation of CS process with fully Lagrangian discretization. To achieve accurate results in similar Lagrangian cases of high plastic deformation, it is suggested to carry out a linear extrapolation to "zero element size" [1,65,66]. Since the deposit was formed in the Eulerian domain, elements of 2 μm were selected as the optimal mesh size to balance the accuracy and computation costs.

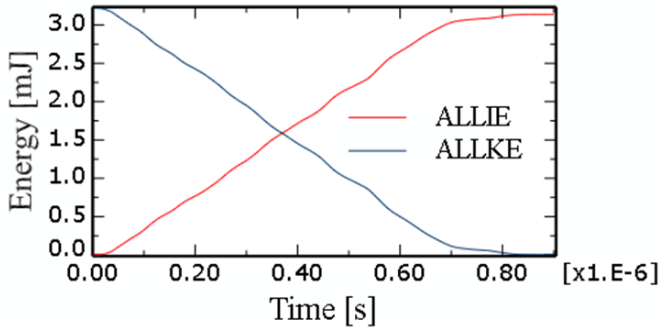

Figure 6: Kinetic (ALLKE) and Internal energy (ALLIE) variation for the whole model during the entire simulation

Figure 6 shows the plot of kinetic and internal energy variation upon impact and during powder deformation. During the simulation, the kinetic energy is almost all transformed in internal energy with a constant and stable trend showing the stability of the solution.

5 Experimental tests

Computational cost and available FE modelling methods prohibit the simulation of CS phenomenon in macro-scale. However, it is still possible to compare the behaviour observed in the simulated deposit at micro-scale with the data acquired from actual CS samples. To that aim, a CS sample of Al-Ti (50% W/W or equally 62.5% V/V of Al) mixture was prepared considering an Al annular substrate. The deposit was obtained using Impact Spray System 5/8 with OUT1 nozzle, operating at 30 bar and 500° C with nitrogen as the propellant gas; these are the same parameters used in the development of the numerical model. The feedstock particle size distributions were those listed in Table 6. Sample's cross section was cut, englobed in cold resin, ground and polished consecutively with refined polishing papers, diamond pastes, and finally with a colloidal silica suspension. The prepared surface of the sample, which represents a cross section of the deposit and substrate, was then examined with SEM Zeiss Evo 50. Image binarization algorithms from ImageJ software [67] were used to locate and define the amount of Al, Ti and pores in the SEM sections.

6 Results

6.1 Numerical simulations

Multiple simulations were conducted considering the following volume fractions of 30, 40, 50, and 70% for the sacrificial material both in Ti-Cu and Ti-Al blends. The final deposits with the obtained stress, strain, and temperature fields for the models with 50/50% volumetric mixture of Ti and sacrificial material are shown in the Figures 7 to 15. It should be noted that Figures 9 and 11 correspond to the variation of stress, strain and temperature along a path through the deposit thickness. For these two diagrams, the path is selected in a way that it does not pass across any pores. The paths are showed in Figure 8 and 10.

The high velocity impact resulted in high deformations. The soft particles (sacrificial material) were severely deformed, showing higher PEEQ than the harder Ti particles. On the other hand, the Ti particles experienced much higher stresses due to its higher stiffness and melting temperature. Indeed, the sacrificial materials' temperature stayed quite close to their melting temperature, reducing their stiffness and therefore stress, according to Eq. 2. Generally, the deformation was more concentrated near the particles' boundary. These high deformations were made possible because of the higher temperature at the particles' interface, which was increased as a result of the heat produced through

friction.

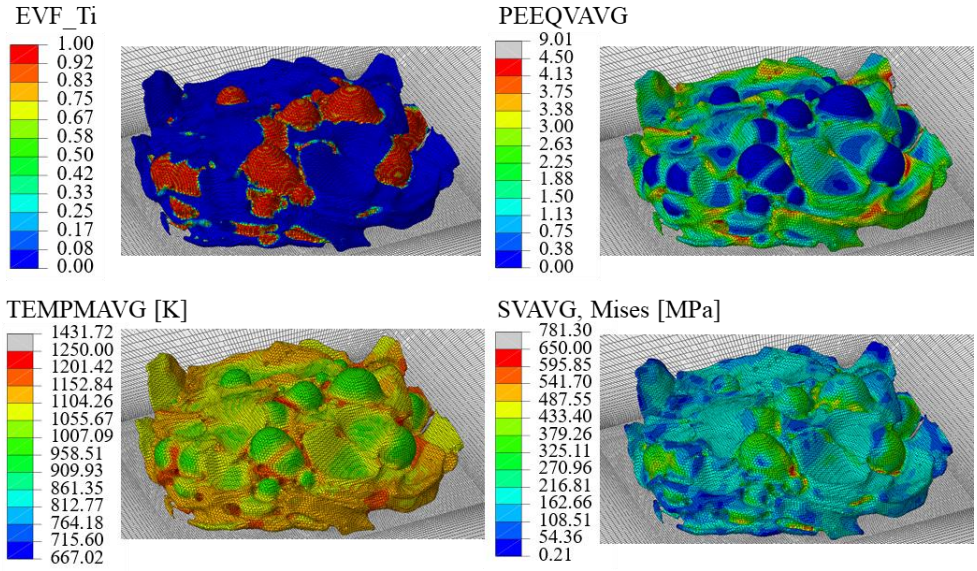

Figure 7. The top view of Ti-Cu 50/50% V/V deposit, representing the Ti volume fraction (EVF_Ti) in which the red region consists of Ti and the blue one of Cu, temperature (TEMPMAVG [K]), PEEQ (PEEQVAVG) and the Von-Mises stress (SVAVG [MPa])

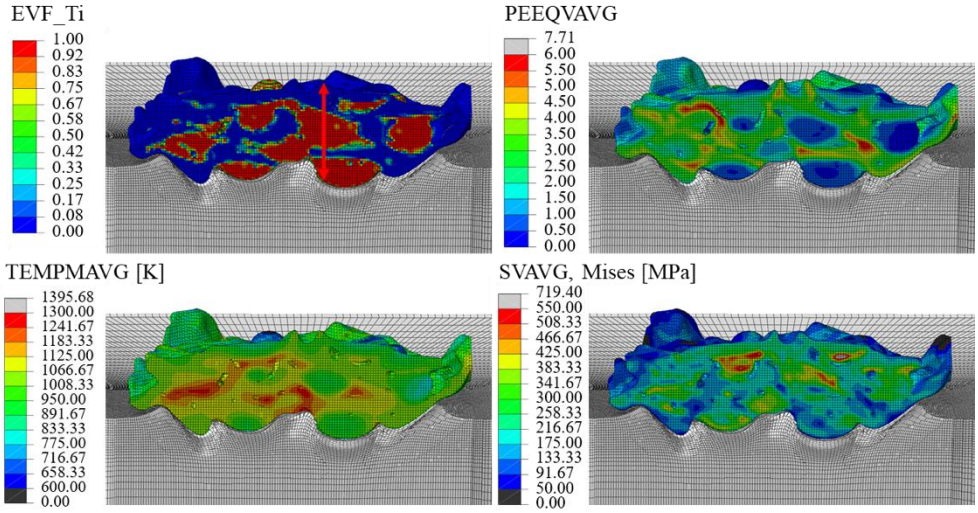

Figure 8. The central section of the Ti-Cu 50/50% V/V deposit. On the top left image showing the Ti volume fraction (EVF_Ti) in which the red region consists of Ti and the blue one of Cu. On the same image the red arrow indicates the path of extracted results presented in Figure 9

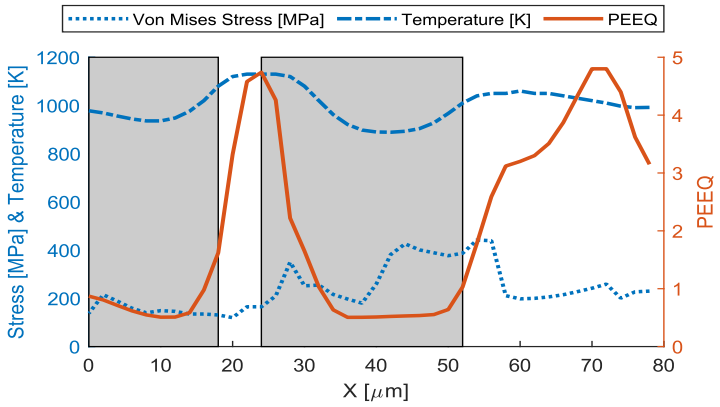

Figure 9. Variations of stress, strain and temperature along the coating thickness (X) of the Ti-Cu 50/50% V/V

deposit. The gray background indicates the Ti, and the white one Cu. X=0 is at the substrate level. The analysed vertical path passing through the particles of each material is shown in Figure 8

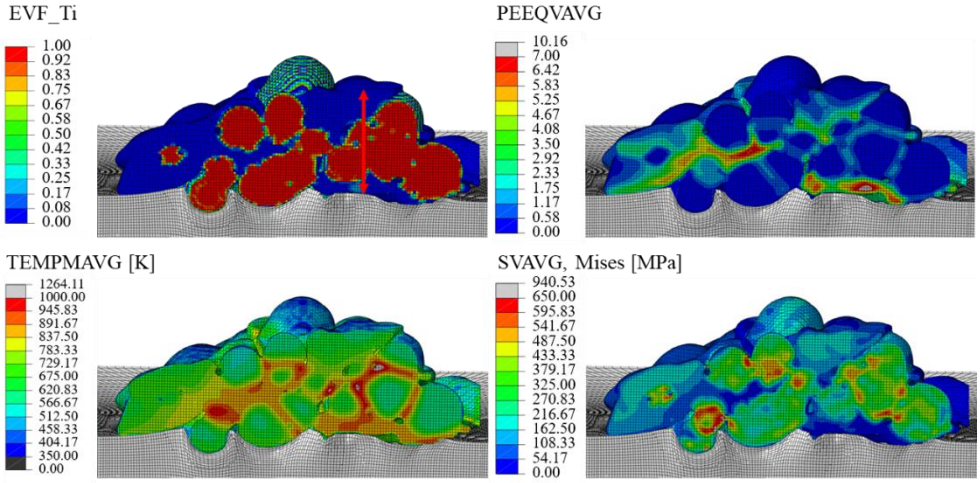

Figure 10. Central section of the TiAl 50/50% V/V deposit. On the top left image showing the Ti volume fraction (EVF_Ti) in which the red region consists of Ti and the blue one of Al. On the same image the red arrow indicates the path of extracted results presented in Figure 11

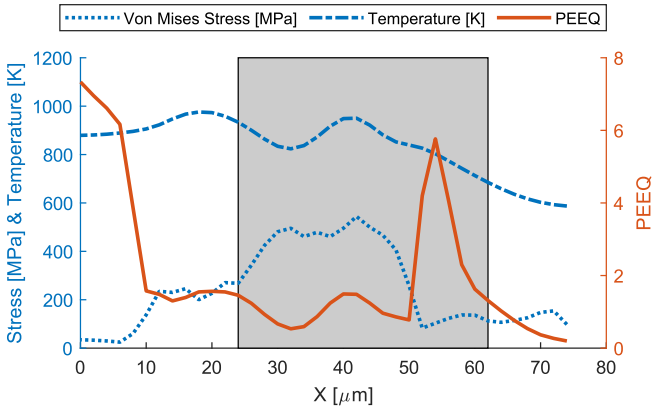

Figure 11. Variations of stress, strain and temperature along the coating thickness (X) of the Ti-Al 50/50% V/V deposit. The gray background indicates the Ti, and the white one Al. X=0 is at the substrate level. The analysed vertical path passing through individual particles is shown in Figure 10

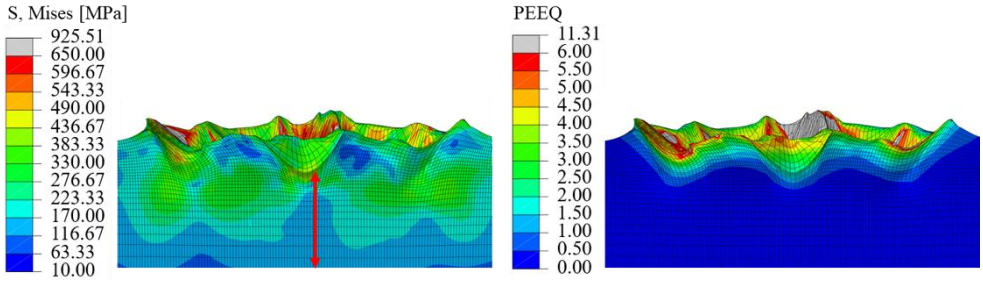

Figure 12. Central section of the Ti-Cu 50/50% V/V corresponding substrate. the red arrow passing through the substrate in the left figure indicates the path of extracted results presented in Figure 14

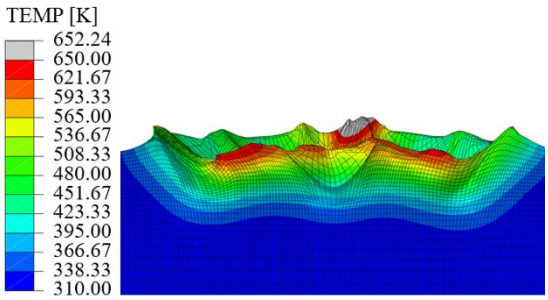

Figure 13. Temperature field of the central section of the TiCu 50/50% V/V corresponding substrate

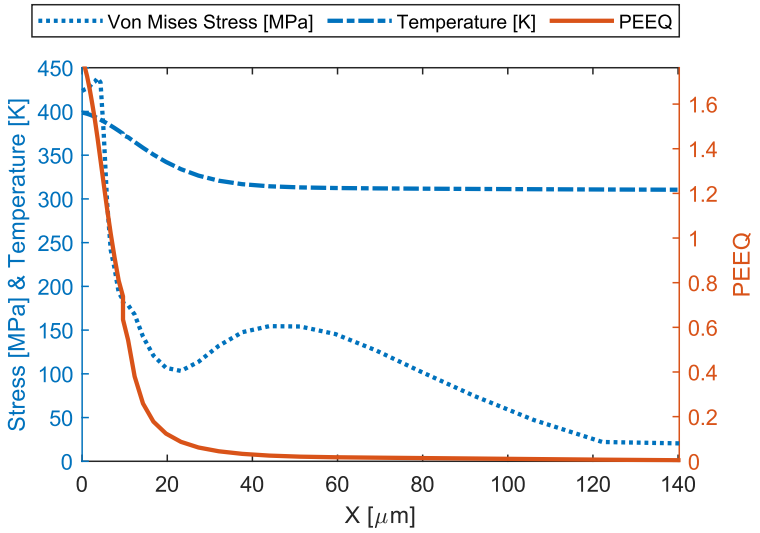

Figure 14. Variations of Von-Mises stress, strain and temperature along the substate thickness (X) of the Ti-Cu 50/50% V/V deposit. X=0 is at the substrate level. The analysed vertical path passing through the substrate is shown in Figure 12

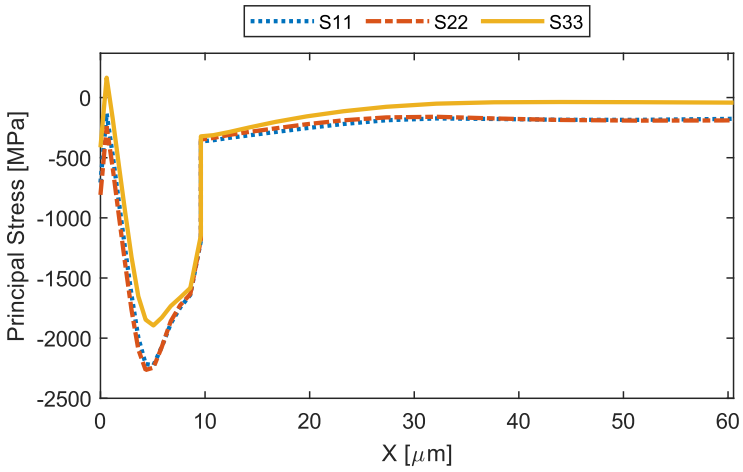

Figure 15. Variations of principal stresses along the substate thickness (X) of the Ti-Cu 50/50% V/V deposit. X=0 is at the substrate level and S33 orthogonal to the substrate surface. The analysed vertical path passing through the substrate is shown in Figure 12

The overall trend of variation of principal stresses through substrate thickness in Figure 15- an initial compressive stress later compensated by a tensile stress- is in accordance with the expected behaviour due to the peening effect of subsequent particles impacting the substrate surface. However, it should be noted that, as discussed before, the sudden stress variation in Figure 15 could be partly associated with the relatively rough mesh size that was considered for the substrate model.

The outputs of the simulations were further elaborated using an ad-hoc Python script, developed to perform in-depth analysis on the topological indices of the deposits. For this post-processing step, the

final state of deformed deposit within the Eulerian domain was imported into the Python code in the form of a 3D NumPy array [68]. This was possible since the deposit in the Eulerian domain was meshed with a regular and non-deformable grid, elements of which had a cubic shape with 2 μm side/mesh size. Therefore, the Eulerian mesh could be considered like a 3D matrix where each mesh element corresponded to a matrix element/voxel in the same exact location in the space. Each element in the coating has a triplet of Euclidean spatial coordinate (X_{el}, Y_{el}, Z_{el}) that can be associated to a triplet of matrix indexes (i, j, k). This association was performed with the following equations:

$$\begin{cases} i = \dfrac{X_{el} - X_{min}}{mesh\ size} \\ j = \dfrac{Y_{el} - Y_{min}}{mesh\ size} \\ k = \dfrac{Z_{el} - Z_{min}}{mesh\ size} \end{cases} \quad (6)$$

Where X_{min}, Y_{min} and Z_{min} were the lowest X_{el}, Y_{el} and Z_{el} dimensions among all the imported elements and the "mesh size" was equal to 2 μm.
Once each mesh element ID was associated to an array in a 3D matrix, it was possible to construct a matrix (3D NumPy array) with each voxel containing the material (Ti or Al/Cu or void) that was dominant in the associated mesh element. Moreover, another 3D-array storing the local PEEQ value was constructed. These arrays were analysed mostly with the Scikit-Image [69] and the PoreSpy [70] libraries. The sacrificial materials (Cu and Al) were removed in an approach, which simulated the chemical etching process, i.e., eliminating the zones that were directly or intermediately connected to the surface of the deposit. In this way, the sacrificial material that was fully surrounded by Ti and thus not accessible to the chemical solution, was not removed from the deposit, making the removal process as realistic as possible. To that aim, all the sacrificial material voxels were grouped in "bodies". Each body was made of all the neighbouring voxels of the same material. For this purpose, the 26-connectivity approach was implemented. In this approach each voxel is considered neighbour to any pixel that touches one of their faces, edges, or corners (Figure 16) [71].

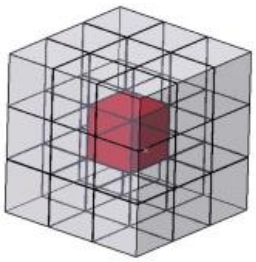

Figure 16. Schematic description of 26-connectivity concept: all the 26 grey voxels are 26-connected to the central red voxel [71]

Following this approach, successively, only the sacrificial material bodies directly in contact with the external environment were transformed into pores (empty voxels), leaving the blind ones intact.
Several parameters were considered as qualitative indices and were calculated for each deposit (Tables 8 and 9). All the considered index parameters are briefly defined as follows:

- Porosity (%): indicates the porosity of the Ti deposit after removal of the sacrificial material. It is calculated as the internal pore volume divided by the total deposited volume.
- Connected Ti (%): indicates the volumetric percentage of the Ti connected material that forms a single body. This parameter serves as an interconnectivity index for the porous deposit. A value lower than 99% indicates that some Ti deposited particles were isolated by the sacrificial material, and thereby were not in contact with the rest of the porous structure.
- Connected pores (%): presents the volumetric percentage of the connected pores. This value indicates the degree of interconnectivity between the empty spaces in the structure.
- Remaining Al/Cu (%): indicates the volumetric percentage of the sacrificial material that remained in the deposit after the simulated etching. A none-zero value is indicative of some sacrificial material being englobed by Ti.

- Connectivity density (1/μm^3) indicates the number of connections in a given volume. Technically, it is the ratio of the connectivity number β_1 of the etched deposit to its volume. β_1 is the first Betty number that indicates the number of the handle-like structures in a body. In other words, it is the maximum number of cuts that can be made without dividing a body into two separate pieces. It is calculated using the Euler-Poincard formula and the Alexander duality theorem [71–73]. More information on the evaluation of this index can be found in the supplementary data.

Table 8: Topological indexes extracted for the porous structure obtained from Ti-Al deposits

Al Vol%	30%	40%	50%	70%
Porosity%	26.67	37.02	51.74	65.00
Connected Ti%	99.96	99.12	99.58	59.96
Connected pores%	96.24	98.42	99.69	99.91
Remaining Al%	0.2	0.11	0.02	0
Connectivity density [1/10^5 μm^3]	10.21	11.92	10.49	8.03

Table 9: Topological indexes extracted for the porous structure obtained from Ti-Cu deposits

Cu Vol%	30%	40%	50%	70%
Porosity%	27.03	36.27	48.22	66.81
Connected Ti%	99.94	99.63	99.11	95.68
Connected pores%	96.49	98.83	99.86	99.70
Remaining Cu%	0.15	0.07	0.01	0
Connectivity density [1/10^5 μm^3]	9.78	11.94	14.46	11.14

Figure 17 compares the statistical distribution of PEEQ for Ti particles in Ti-Cu and Ti-Al simulations considering 30% V/V for the corresponding sacrificial powder, as a representative case. The area inside the box plot of Figure 17 shows the values between the first and the third quartile, while the orange horizontal line indicates the median value. The coloured area within the violin plot represents the probability density function. The results indicate that Ti particles in the Ti-Cu deposits exhibited higher particle deformation, which can be interpreted also as higher Ti particle bonding compared to the Ti-Al case.

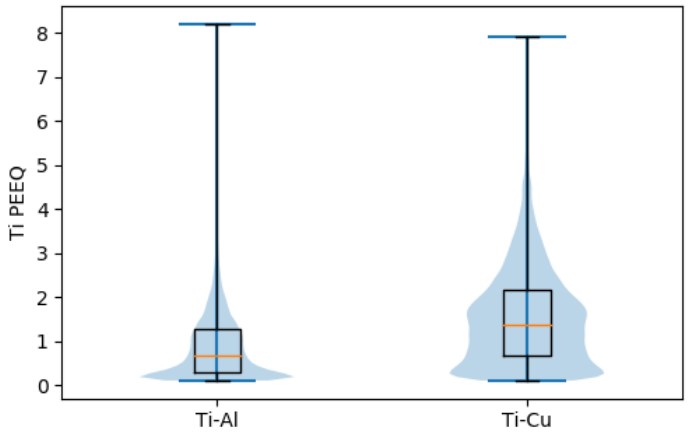

Figure 17. Statistical distribution of PEEQ of Ti particles for Ti-Al and Ti-Cu deposits considering 30% V/V of the corresponding sacrificial powders

As pointed out before, to reduce the computational costs and maintain the accuracy of the results, the model and the resulting deposit in these series of analyses were developed at micro-scale using model with 2 μm of mesh size. Just to make a better comparison with the preliminary experimental findings and to provide a clearer visual perspective of the obtained porous structures, a larger model with coarser mesh of 3.5 μm was constructed and analysed using different Ti-Cu compositions. These models contained about 600 Ti particles and the corresponding required number of Cu. The higher number of particles required much larger Lagrangian and Eulerian domains, i.e., a 0.3×0.3×2.5 mm Eulerian domain and a 0.9×0.9×0.3 mm Lagrangian substrate in case of the 50-50% V/V Ti-Cu. Figure 18

demonstrates the hereby described deposit models, after removing the sacrificial powder, i.e., Cu.
The deposit sections displayed in Figures 18 and 19 were achieved by applying view cuts on all sides of the Eulerian domain, to achieve a better view of the internal arrangement of pores and particle deformations. So, the sharp cut sections on different particles should not be mistaken for the material outflow, the absence of which was discussed in section 4.1.

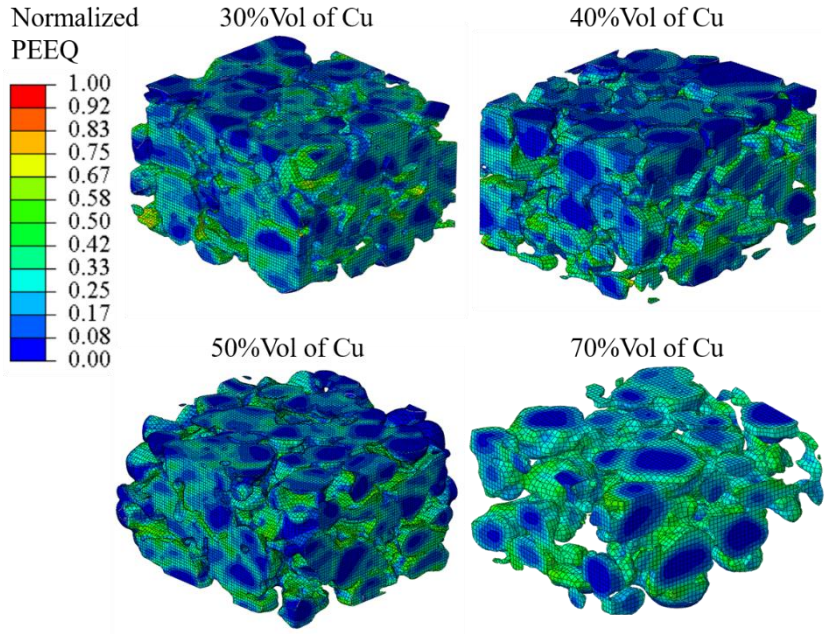

Figure 18. Normalized PEEQ contour of cubic Ti porous structures obtained using different volume fractions of sacrificial powder (Cu)

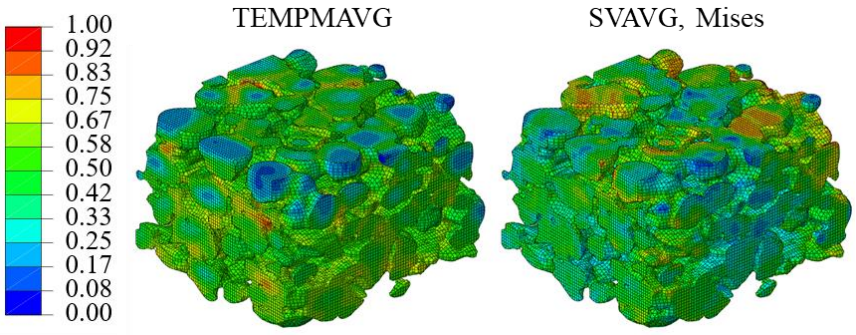

Figure 19. Normalized Temperature (TEMPMAVG) and Von-Mises stress (SVAVG) contour of cubic Ti porous structures for the model with 50% V/V of Ti and Cu

It is worth mentioning that the SVAVG contour in Figure 19 reflects only the volume fraction average of Von-Mises stress for the voxels that contain any remaining material after etching from the initial deposition simulation. So, the presented values do not reflect the re-evaluated magnitude of stress after removing the accessible sacrificial material from the deposit, which is not a part of the current study.

6.2 Experimental data

Figure 20 shows representative processed SEM images of the Al-Ti sample, obtained using 50% W/W feedstock, at different enlargements. The images were analysed to calculate the macro-porosity and approximate volumetric content of each constituent phase.
The images exhibit an Al matrix enclosing some spherical Ti particles, few of which are touching and forming small agglomerates. The overall deposit is homogeneous with well dispersed Ti particles in the Al matrix. The Ti particles exhibit minor or negligible deformation, retaining the original spherical shape of the powder particles. Analysis of the processed SEM images determined that Al constituted a mean value of 73.1% V/V, equivalent to 62.2% W/W of the whole deposit.

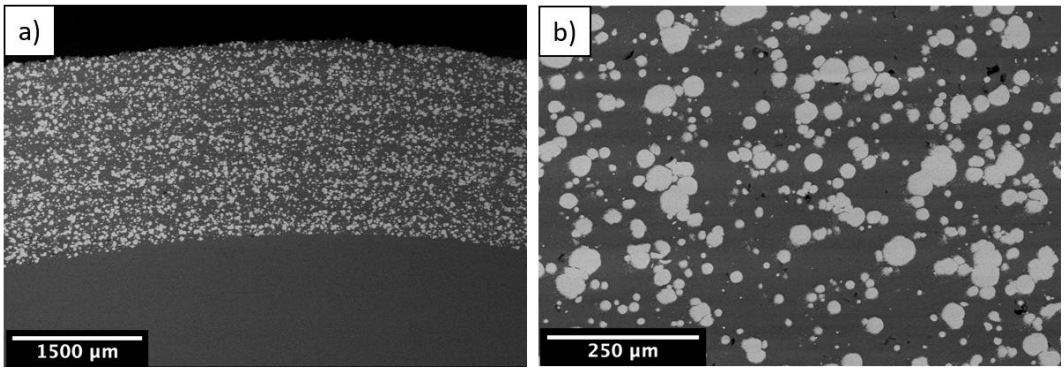

Figure 20. SEM images at (a) 75x and (b) 500x magnification from the Ti-Al 50% W/W deposit; the darker matrix consists of Al, and the lighter one of Ti particles

A linear arrangement of the deposited particles is identifiable in Figure 20 (a). This can be explained by the fact that the powders of two materials were not pre-mixed prior to entering the gas flow. Instead, each material powder was incrementally injected into the conveyer gas using separate feeders. The feed rate was controlled by the rotation velocity of a feeder disk containing discretely spaced holes, which explains the non-homogeneous mixture of the powders and the resultant distinguishable deposit layers.

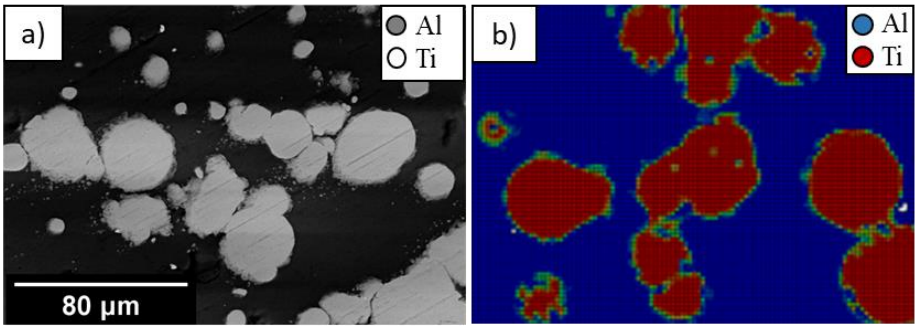

Figure 21. a) A representative cross-sectional SEM image of the sample, b) FE cross section Ti-Al deposit (2 µm of mesh size); both the sample and FE deposit have around 70% V/V of Al phase and both the images have the same scale bar

Figure 21 displays a qualitative comparison between the features on the cross-section of the deposited sample and the one obtained from the numerical model; the numerical model was developed with parameters equivalent to those used in the experiment considering the same volume fractions of deposited powder mixture (based on the effective DE calculated from the SEM image analysis). The cross-sectional views show similar results in terms of qualitative deformation and morphology of Ti particles.

7 Discussion

Herein, multi-material CS deposition was modelled considering the peculiarities of mixed feedstock, and the corresponding assignment of particle velocity and temperature as a function of main process parameters. In each case, one constituent material in the mixture, either Al or Cu, was considered as the sacrificial constituent. The sacrificial material was removed in a novel post-processing step that numerically simulated the systematic removal of the sacrificial material to achieve a porous Ti deposit. The obtained results indicated that the soft Al and Cu particles deformed heavily during deposition, filling almost all the inter-particle spaces that would have been otherwise prominent in a pure Ti deposit, leading to multi-material deposits with low porosity.

The extent of deformation in terms of PEEQ of the Ti deposited particles was considered as an index of the deposit's strength[2]. Thus, it was postulated that the higher Ti particle deformation in Ti-Cu mixtures could lead to higher particle to particle bonding and therefore increased CS deposit strength (Figure 17). There are two main contributing factors to this increased deformation. One is the higher stagnation temperature and pressure that can be considered for Ti-Cu simulation, leading to higher particle velocity and temperature. The second reason is the higher density, and hence, inertia of Cu

particles when compared to that of Al ones with equal size (Cu density = 8.96 g/cm^3, and Al density = 2.7 g/cm^3). Combination of higher particle impact momentum (higher velocity and density/inertia) and higher thermal softening of Cu particles leads to higher deformation and PEEQ values in the Ti-Cu deposits compared to Ti-Al. It is worth noting that when mixing Al with Ti powder to serve as sacrificial material, it is challenging to achieve high particle deformation in the Ti phase (Figure 17), due to the lower stagnation temperatures limited by the risk of nozzle clogging by Al particles.

As expected, increasing the amount of sacrificial material led to a notable increase in the porosity after simulating the etching step, confirming that the deposit porosity is mainly induced by the sacrificial material. Generally, in cases with a sacrificial material powder content less than 50% V/V, all the Ti particles were interconnected, but at higher concentrations of sacrificial powder, disconnections between Ti particles started to appear. This low Ti interconnectivity was particularly evident in the case of Ti-Al deposit with 70% V/V of sacrificial material (Figure 21). Porosity predictably exhibited an opposite trend, i.e., pores were largely interconnected in cases with higher sacrificial material contents higher than 40% V/V, below which they were organized in the form of isolated unconnected groups.

When analyzing the remaining Ti structures, considering both pore and Ti particles' connectivity, an optimum state was achieved with 50% V/V of Cu in the Ti-Cu deposit, and 40% V/V of Al in Ti-Al one. Above these levels, there will be a notable decline in Ti particle interconnectivity, and below them the pore interconnectivity decreased. The difference between the optimum sacrificial powder content for these two cases (Al vs. Cu) can be associated with the intrinsic difference in their deformability and deposition parameters. These differences led to variations of Ti particles' deformation between the two models. Hence, to achieve a certain level of deformation and in turn, interconnection between the deformed Ti particles, different values of each sacrificial material were required.

Generally, the residual amount of Al or Cu in the deposit after the simulated chemical etching was very low. This can be correlated to the relatively small size of the modelled deposits, which results in a large percentage of the sacrificial particles being connected to the external surface of deposit. In case of a thicker depositions, the total amount of entrapped sacrificial material is expected to be higher. For that matter, specific deposition strategies should be adopted to gain more control on the particle placement and modulate the connectivity of the sacrificial material within the deposit bulk.

Inspection of the experimentally deposited sample's cross-section revealed that Al constituted about 73% V/V of the deposit, despite the 62.5% V/V of the feedstock powder. This variation indicates the higher compositional yield for Al compared to Ti powders in the deposit, which is in line with the higher DE expected for more deformable Al particles. Comparison of the SEM cross-sectional images and the deformation contour of the simulation using the same percentage of powder volume fractions, exhibited quite dense deposits in both cases as a result of the high deformation of Al, which filled the otherwise empty spaces between Ti particles. The Al yield in the deposited sample is considerably higher than the proposed optimum amount of 40% V/V and chemical etching will not lead to an interconnected porous Ti structure. This observation is in agreement with the observed trend in the FE data and highlight the necessity to consider the effective DE of each individual phase in the blend, while designing experiments to evaluate the correlation between the feedstock volume fraction and the compositional yield in multi-material deposits, based on the thermomechanical properties of the constituent phases. Future experiments will be performed to quantitatively compare the contribution of different feedstock and validate the proposed computations framework for different material combinations.

8 Conclusions

A detailed numerical framework was presented for modelling multi-material cold spray deposition aiming to obtain porous cold spray deposits through introduction of a sacrificial powder and characterize their topological features. The effects of the sacrificial material type and volume fraction were investigated highlighting the capability of the developed method to evaluate the optimum condition. Based on the obtained results the following conclusions can be drawn:

- The intricate finite element model described here has proven to be a powerful tool able to simulate the multi-particle cold spray deposition of a blended feedstock, while considering particle size distribution and the individually assigned velocities and temperatures.
- The sacrificial material was removed in a novel post-processing step that numerically simulated the systematic removal of the sacrificial material (simulating the chemical etching step) to

achieve a porous Ti deposit.

- The proposed modelling scheme was able to successfully provide the state of stress, temperature, and strain in the final deposit, while allowing to identify and separately analyse the effect of sacrificial powder content and material on the Ti particles deformation, and porosity.
- A strong and well-interconnected porous Ti deposit was obtained from 50-50% V/V Ti-Cu feedstock, considering stagnation pressure and temperature of 50 bar and 750 °C, respectively.
- The distribution of plastic strain and stress in the deposit of Ti-Al mixture proved the possibility of obtaining a highly connected and porous Ti deposit, but with lower Ti particle deformation and hence, lower cohesive strength. This was due to the limited stagnation temperatures imposed by the nozzle clogging by Al at higher temperature, that in turn, led to lower Ti particle deformation compared to the Ti-Cu simulation where higher stagnation temperature could be considered.
- Post-processing of the deposits' configuration revealed that in most cases, inclusion of more than 50% V/V of sacrificial powder will result in generation of a segregated Ti structure; on the other hand, in cases with lower than 40% V/V of sacrificial material, the low porosity impeded the formation of internal interconnected pore. These observations led to the conclusion that the optimum porous, interconnected Ti structure would be achieved for values of 40 ~ 50% volume fraction of sacrificial powder.

References

[1] H. Assadi, F. Gärtner, T. Stoltenhoff, H. Kreye, Bonding mechanism in cold gas spraying, Acta Mater. 51 (2003) 4379–4394. https://doi.org/10.1016/S1359-6454(03)00274-X.

[2] S. Bagherifard, A. Heydari Astaraee, M. Locati, A. Nawaz, S. Monti, J. Kondás, R. Singh, M. Guagliano, Design and analysis of additive manufactured bimodal structures obtained by cold spray deposition, Addit. Manuf. 33 (2020) 101131. https://doi.org/https://doi.org/10.1016/j.addma.2020.101131.

[3] S. Bagherifard, M. Guagliano, Fatigue performance of cold spray deposits: Coating, repair and additive manufacturing cases, Int. J. Fatigue. 139 (2020) 105744. https://doi.org/https://doi.org/10.1016/j.ijfatigue.2020.105744.

[4] A. V Fedorov, N.D. Malmuth, A. Rasheed, H.G. Hornung, Stabilization of Hypersonic Boundary Layers by Porous Coatings, AIAA J. 39 (2001) 605–610. https://doi.org/10.2514/2.1382.

[5] H. Lee, K. Ko, Fabrication of porous Al alloy coatings by cold gas dynamic spray process, Surf. Eng. 26 (2010) 395–398. https://doi.org/10.1179/026708409X12490360426124.

[6] S. Deshpande, A. Kulkarni, S. Sampath, H. Herman, Application of image analysis for characterization of porosity in thermal spray coatings and correlation with small angle neutron scattering, Surf. Coatings Technol. 187 (2004) 6–16. https://doi.org/10.1016/j.surfcoat.2004.01.032.

[7] G. Patents, Patents Surgical prosthetic device with porous metal coating US3855638A, (2020) 1–18.

[8] G. Ryan, A. Pandit, D.P. Apatsidis, Fabrication methods of porous metals for use in orthopaedic applications, Biomaterials. 27 (2006) 2651–2670. https://doi.org/10.1016/j.biomaterials.2005.12.002.

[9] G. Patents, Patents Porous metal coating process and mold therefor US4612160A, (2020).

[10] R.M. Pillar, Surgical prosthetic device or implant having pure metal porous coating, U S Pat. 4,206,516. 12 (1980) 2–4.

[11] S. Bagherifard, J. Kondas, S. Monti, J. Cizek, F. Perego, O. Kovarik, F. Lukac, F. Gaertner, M. Guagliano, Tailoring cold spray additive manufacturing of steel 316 L for static and cyclic load-bearing applications, Mater. Des. 203 (2021) 109575. https://doi.org/10.1016/j.matdes.2021.109575.

[12] H. Lee, feeding Of powder having tWO types Or more MetaS Supplying Of S220 Spraying of Metal pOWCler-gaS mixture through nozzle, 1 (2007).

[13] F.A. Sohag, F.R. Beck, L. Mohanta, F.B. Cheung, A.E. Segall, T.J. Eden, J.K. Potter, Effects of subcooling on downward facing boiling heat transfer with micro-porous coating formed by Cold Spray technique, Int. J. Heat Mass Transf. 106 (2017) 767–780.

https://doi.org/10.1016/j.ijheatmasstransfer.2016.09.091.
[14] J. Sun, Y. Han, K. Cui, Innovative fabrication of porous titanium coating on titanium by cold spraying and vacuum sintering, Mater. Lett. 62 (2008) 3623–3625. https://doi.org/10.1016/j.matlet.2008.04.011.
[15] D. Qiu, M. Zhang, L. Grøndahl, A novel composite porous coating approach for bioactive titanium-based orthopedic implants, J. Biomed. Mater. Res. - Part A. 101 A (2013) 862–872. https://doi.org/10.1002/jbm.a.34372.
[16] W. Li, H. Assadi, F. Gaertner, S. Yin, A Review of Advanced Composite and Nanostructured Coatings by Solid-State Cold Spraying Process, Crit. Rev. Solid State Mater. Sci. 44 (2019) 109–156. https://doi.org/10.1080/10408436.2017.1410778.
[17] C. Sun, X. Zhou, C. Xie, B. Liu, Investigating hard/soft combinations of cold spraying by Eulerian approach, Surf. Eng. 36 (2020) 1049–1057. https://doi.org/10.1080/02670844.2019.1710036.
[18] R. Ghelichi, S. Bagherifard, M. Guagliano, M. Verani, Numerical simulation of cold spray coating, Surf. Coatings Technol. 205 (2011) 5294–5301. https://doi.org/10.1016/j.surfcoat.2011.05.038.
[19] F. Oviedo, A. Valarezo, Residual Stress in High-Velocity Impact Coatings: Parametric Finite Element Analysis Approach, J. Therm. Spray Technol. 29 (2020) 1268–1288. https://doi.org/10.1007/s11666-020-01026-5.
[20] M. Saleh, V. Luzin, K. Spencer, Analysis of the residual stress and bonding mechanism in the cold spray technique using experimental and numerical methods, Surf. Coatings Technol. 252 (2014) 15–28. https://doi.org/10.1016/j.surfcoat.2014.04.059.
[21] G. Shayegan, H. Mahmoudi, R. Ghelichi, J. Villafuerte, J. Wang, M. Guagliano, H. Jahed, Residual stress induced by cold spray coating of magnesium AZ31B extrusion, Mater. Des. 60 (2014) 72–84. https://doi.org/10.1016/j.matdes.2014.03.054.
[22] E. Lin, I. Nault, O.C. Ozdemir, V.K. Champagne, A. Nardi, S. Müftü, Thermo-Mechanical Deformation History and the Residual Stress Distribution in Cold Spray, J. Therm. Spray Technol. 29 (2020) 1424–1436. https://doi.org/10.1007/s11666-020-01034-5.
[23] S. Suresh, S.W. Lee, M. Aindow, H.D. Brody, V.K. Champagne, A.M. Dongare, Mesoscale modeling of jet initiation behavior and microstructural evolution during cold spray single particle impact, Acta Mater. 182 (2020) 197–206. https://doi.org/10.1016/j.actamat.2019.10.039.
[24] X. Song, J. Everaerts, W. Zhai, H. Zheng, A.W.Y. Tan, W. Sun, F. Li, I. Marinescu, E. Liu, A.M. Korsunsky, Residual stresses in single particle splat of metal cold spray process – Numerical simulation and direct measurement, Mater. Lett. 230 (2018) 152–156. https://doi.org/10.1016/j.matlet.2018.07.117.
[25] R. Ghelichi, S. Bagherifard, D. Macdonald, I. Fernandez-Pariente, B. Jodoin, M. Guagliano, Experimental and numerical study of residual stress evolution in cold spray coating, Appl. Surf. Sci. 288 (2014) 26–33. https://doi.org/10.1016/j.apsusc.2013.09.074.
[26] J.M. Schreiber, J.M. Schreiber, Finite element implementation of the preston-tonks-wallace plasticity model and energy based bonding parameter for the cold spray process, (2016).
[27] T. Schmidt, F. Gärtner, H. Assadi, H. Kreye, Development of a generalized parameter window for cold spray deposition, Acta Mater. 54 (2006) 729–742. https://doi.org/10.1016/j.actamat.2005.10.005.
[28] B. Yildirim, S. Muftu, A. Gouldstone, Modeling of high velocity impact of spherical particles, Wear. 270 (2011) 703–713. https://doi.org/10.1016/j.wear.2011.02.003.
[29] J.G. Lee, D.Y. Kim, B. Kang, D. Kim, S.S. Al-Deyab, S.C. James, S.S. Yoon, Thin film metallization by supersonic spraying of copper and nickel nanoparticles on a silicon substrate, Comput. Mater. Sci. 108 (2015) 114–120. https://doi.org/10.1016/j.commatsci.2015.06.016.
[30] D. MacDonald, R. Fernández, F. Delloro, B. Jodoin, Cold Spraying of Armstrong Process Titanium Powder for Additive Manufacturing, J. Therm. Spray Technol. 26 (2017) 598–609. https://doi.org/10.1007/s11666-016-0489-2.
[31] G. Bae, Y. Xiong, S. Kumar, K. Kang, C. Lee, General aspects of interface bonding in kinetic sprayed coatings, Acta Mater. 56 (2008) 4858–4868. https://doi.org/10.1016/j.actamat.2008.06.003.
[32] W.Y. Li, H. Liao, C.J. Li, G. Li, C. Coddet, X. Wang, On high velocity impact of micro-sized

metallic particles in cold spraying, Appl. Surf. Sci. 253 (2006) 2852–2862. https://doi.org/10.1016/j.apsusc.2006.05.126.
[33] F. Delloro, M. Jeandin, D. Jeulin, H. Proudhon, M. Faessel, L. Bianchi, E. Meillot, L. Helfen, A Morphological Approach to the Modeling of the Cold Spray Process, J. Therm. Spray Technol. 26 (2017) 1838–1850. https://doi.org/10.1007/s11666-017-0624-8.
[34] A. MANAP, K. OGAWA, T. OKABE, Numerical Analysis of Interfacial Bonding of Al-Si Particle and Mild Steel Substrate by Cold Spray Technique Using the SPH Method, J. Solid Mech. Mater. Eng. 6 (2012) 241–250. https://doi.org/10.1299/jmmp.6.241.
[35] A. Manap, O. Nooririnah, H. Misran, T. Okabe, K. Ogawa, Experimental and SPH study of cold spray impact between similar and dissimilar metals, Surf. Eng. 30 (2014) 335–341. https://doi.org/10.1179/1743294413Y.0000000237.
[36] X. Song, K.L. Ng, J.M.K. Chea, W. Sun, A.W.Y. Tan, W. Zhai, F. Li, I. Marinescu, E. Liu, Coupled Eulerian-Lagrangian (CEL) simulation of multiple particle impact during Metal Cold Spray process for coating porosity prediction, Surf. Coatings Technol. 385 (2020) 125433. https://doi.org/10.1016/j.surfcoat.2020.125433.
[37] Z. Zhu, S. Kamnis, S. Gu, Numerical study of molten and semi-molten ceramic impingement by using coupled Eulerian and Lagrangian method, Acta Mater. 90 (2015) 77–87. https://doi.org/10.1016/j.actamat.2015.02.010.
[38] S. Weiller, F. Delloro, P. Lomonaco, M. Jeandin, C. Garion, A finite elements study on porosity creation mechanisms in cold sprayed coatings, Key Eng. Mater. 813 KEM (2019) 358–363. https://doi.org/10.4028/www.scientific.net/KEM.813.358.
[39] S. Yin, X.F. Wang, B.P. Xu, W.Y. Li, Examination on the calculation method for modeling the multi-particle impact process in cold spraying, J. Therm. Spray Technol. 19 (2010) 1032–1041. https://doi.org/10.1007/s11666-010-9489-9.
[40] K.F. Khaled, Corrosion control of copper in nitric acid solutions using some amino acids - A combined experimental and theoretical study, Corros. Sci. 52 (2010) 3225–3234. https://doi.org/10.1016/j.corsci.2010.05.039.
[41] K.F. Khaled, S.A. Fadl-Allah, B. Hammouti, Some benzotriazole derivatives as corrosion inhibitors for copper in acidic medium: Experimental and quantum chemical molecular dynamics approach, Mater. Chem. Phys. 117 (2009) 148–155. https://doi.org/10.1016/j.matchemphys.2009.05.043.
[42] G. Welsch, R. Boyer, E.W. Collings, Materials properties handbook: Titanium alloys, 2nd ed, 1998.
[43] J. Xie, D. Nelias, H. Walter-Le Berre, Y. Ichikawa, K. Ogawa, Numerical simulation of the cold spray deposition process for aluminium and copper, ASME 2012 11th Bienn. Conf. Eng. Syst. Des. Anal. ESDA 2012. 1 (2012) 109–111. https://doi.org/10.1115/ESDA2012-82107.
[44] J. Xie, Simulation of Cold Spray Particle Deposition, (2014).
[45] D. Nélias, J. Xie, H. Walter-Le Berre, Y. Ichikawa, K. Ogawa, Simulation of the Cold Spray Deposition Process for Aluminum and Copper using Lagrangian, ALE and CEL Methods, Thermomechanical Ind. Process. Model. Numer. Simul. 9781848213 (2014) 321–358. https://doi.org/10.1002/9781118578759.ch7.
[46] J. Xie, D. Nélias, H.W. Le Berre, K. Ogawa, Y. Ichikawa, Simulation of the cold spray particle deposition process, J. Tribol. 137 (2015) 1–15. https://doi.org/10.1115/1.4030257.
[47] R. Menikoff, Complete Mie-Gruneisen Equation of State, n.d.
[48] ABAQUS Inc., Abaqus documentation 2017, n.d.
[49] T. Hussain, D.G. Mccartney, P.H. Shipway, T. Hussain, D.G. Mccartney, P.H. Shipway, Bonding between aluminium and copper in cold spraying : story of asymmetry Bonding between aluminium and copper in cold spraying : story of asymmetry, 0836 (2013). https://doi.org/10.1179/1743284712Y.0000000051.
[50] K.S.V. Sekar, M.P. Kumar, Finite Element Simulations of Ti6Al4V Titanium Alloy Machining to Assess Material Model Parameters of the Johnson-Cook Constitutive Equation, XXXIII (2011) 203–211.
[51] M. The, H. Strain, R. Behavior, O.F. Titanium, U.B. Impact, Impact engineering modeling the high strain rate behavior of titanium, (2001).
[52] MPDB Software, (n.d.).
[53] E.A. Deulin, Mechanics and Physics of Precise Vacuum Mechanisms, n.d.

[54] P.J. Blau, Friction Science and Technology: From Concepts to Applications, Second Edition -, (n.d.).
[55] S. Matsumoto, Y. Takashima, Droplet Size Distribution in Spray, Chem. Eng. 33 (1969) 357-360,a1. https://doi.org/10.1252/kakoronbunshu1953.33.357.
[56] I. Brezáni, F. Zeleňák, Improving the effectivity of work with rosin-rammler diagram by using MATLAB® GUI tool, Acta Montan. Slovaca. 15 (2010) 152–157.
[57] A. Gupta, D.S. Yan, Particle Size Estimation and Distributions, 2006. https://doi.org/10.1016/b978-044451636-7/50003-6.
[58] K.N. Ramakrishnan, Modified Rosin Rammler equation for describing particle size distribution of milled powders, J. Mater. Sci. Lett. 19 (2000) 1903–1906. https://doi.org/10.1023/A:1006742928764.
[59] KSS Kinetic Spray Solutions – Simulation in Gas Dynamic Cold Spraying, (n.d.).
[60] H. Assadi, T. Schmidt, H. Richter, J.O. Kliemann, K. Binder, F. Gärtner, T. Klassen, H. Kreye, On parameter selection in cold spraying, J. Therm. Spray Technol. 20 (2011) 1161–1176. https://doi.org/10.1007/s11666-011-9662-9.
[61] T. Schmidt, H. Assadi, F. Gärtner, H. Richter, T. Stoltenhoff, H. Kreye, T. Klassen, From particle acceleration to impact and bonding in cold spraying, J. Therm. Spray Technol. 18 (2009) 794–808. https://doi.org/10.1007/s11666-009-9357-7.
[62] Python Documentation, (2020).
[63] X. Wang, B. Zhang, J. Lv, S. Yin, Investigation on the Clogging Behavior and Additional Wall Cooling for the Axial-Injection Cold Spray Nozzle, J. Therm. Spray Technol. 24 (2015) 696–701. https://doi.org/10.1007/s11666-015-0227-1.
[64] A. Sova, D. Pervushin, I. Smurov, Development of multimaterial coatings by cold spray and gas detonation spraying, Surf. Coatings Technol. 205 (2010) 1108–1114. https://doi.org/10.1016/j.surfcoat.2010.07.092.
[65] S. Bagherifard, R. Ghelichi, M. Guagliano, A numerical model of severe shot peening (SSP) to predict the generation of a nanostructured surface layer of material, Surf. Coatings Technol. 204 (2010) 4081–4090. https://doi.org/10.1016/j.surfcoat.2010.05.035.
[66] R. Giusti, S. Vezzù, G. Lucchetta, Wear-resistant cobalt-based coatings for injection moulds by cold spray, Surf. Eng. 32 (2016) 677–685. https://doi.org/10.1080/02670844.2016.1177257.
[67] C.A. Schneider, W.S. Rasband, K.W. Eliceiri, NIH Image to ImageJ: 25 years of image analysis, Nat. Methods. 9 (2012) 671–675. https://doi.org/10.1038/nmeth.2089.
[68] NumPy documentation, (n.d.).
[69] S. Van Der Walt, J.L. Schönberger, J. Nunez-Iglesias, F. Boulogne, J.D. Warner, N. Yager, E. Gouillart, T. Yu, Scikit-image: Image processing in python, PeerJ. 2014 (2014) e453. https://doi.org/10.7717/peerj.453.
[70] PoreSpy Documentation — PoreSpy documentation, (n.d.).
[71] J. Toriwaki, T. Yonekura, Euler number and connectivity indexes of a three dimensional digital picture, Forma-Tokyo-. 17 (2002) 183–209.
[72] A. Odgaard, H.J.G. Gundersen, Quantification of connectivity in cancellous bone, with special emphasis on 3-D reconstructions, Bone. 14 (1993) 173–182. https://doi.org/10.1016/8756-3282(93)90245-6.
[73] A. Gonzalez-lorenzo, M. Juda, A. Bac, J. Mari, A. Gonzalez-lorenzo, M. Juda, A. Bac, J. Mari, P.R. Fast, Fast , Simple and Separable Computation of Betti Numbers on Three-dimensional Cubical Complexes To cite this version : HAL Id : hal-01341014 Fast , Simple and Separable Computation of Betti Numbers on Three-dimensional Cubical Complexes, (2017).